$[2\pi + 2\pi]$ Photocycloaddition of Enones to Single-Walled Carbon Nanotubes Creates

Fluorescent Quantum Defects

Xiaoyun He[†], Ilia Kevlishvili[†], Katherina Murcek[‡], Peng Liu^{†,‡}, Alexander Star^{‡,§,*}

†Department of Chemistry, ‡Department of Chemical and Petroleum Engineering, and

§Department of Bioengineering, University of Pittsburgh, Pittsburgh, Pennsylvania 15260,

United States

Abstract

Single-walled carbon nanotubes (SWCNTs) have been widely applied in biomedical fields such as drug delivery, biosensing, bioimaging, and tissue engineering. Understanding their reactivity with biomolecules is important for these applications. We describe here a photo-induced cycloaddition reaction between enones and SWCNTs. By creating covalent and tunable sp³ defects in the sp² carbon lattice of SWCNTs through $[2\pi + 2\pi]$ photocycloaddition, a bright red-shifted photoluminescence was gradually generated. The photocycloaddition functionalization was demonstrated with various organic molecules bearing enone functional group, including biologically important oxygenated lipid metabolites. The mechanism of this reaction was studied empirically and using computational methods. Density functional theory (DFT) calculations were employed to elucidate the identity of the reaction product and understand the origin of different substrate reactivities. The results of this study can enable

engineering of the optical and electronic properties of semiconducting SWCNTs and provide understanding into their interactions with lipid biocorona.

Keywords: SWCNTs, enones, oxygenated lipid mediators, photocycloaddition, defect-induced NIR PL, DFT calculations

Semiconducting single-walled carbon nanotubes (SWCNTs) exhibit chiralitydependent near-infrared (NIR) photoluminescence (PL) when their bundles are exfoliated by suspension using surfactants.^{1, 2} Each single-chirality semiconducting SWCNT displays characteristic E₂₂ excitation – E₁₁ emission peak, related to its optical transition between corresponding van Hove singularities. In addition to this band-gap fluorescence, the emergence of a red-shifted fluorescence emission, designated as E_{11}^- or E_{11}^* , was reported.³⁻⁵ The activation of the red-shifted PL has been achieved by reactions with ozone, 3, 6 lipid hydroperoxide,⁷ hypochlorite,⁸ alkylation,^{4, 9-14} diazonium chemistry,^{5, 15, 16} guanine nucleobases, ¹⁷ and other chemical treatments. ¹⁸⁻²³ This emission is a single-photon in nature, ²⁴ can facilitate up-conversion²⁵ and be generated from trions trapped at chemical sites at room temperature. 13, 14 These features enable the applications of functionalized-SWCNTs as promising fluorescent probes with excitation and emission in the NIR region well suited in noninvasive in vivo detection and bioimaging. Additional applications include single-photon emission at room temperature in photonic devices, ²⁶⁻²⁸ as well as chemical sensing. ²⁹ However, even though the mechanism of this optical behavior has been extensively studied, 30, 31 the chemical types of created quantum defects are still limited.^{22, 23} Beyond oxygen-containing defects on the SWCNTs, $^{3, 6-8}$ alkyl $^{4, 9-14}$ and aryl $^{5, 15, 16, 18-21}$ groups have been also shown to generate E₁₁⁻ emission. Among them, only few studies 10, 15, 18-20 reported the creation of the fluorescent quantum defects other than oxygen by means of photochemical reaction activated under either E₂₂ transition of nanotubes or UV light.

Polyunsaturated fatty acids (PUFA) are one of the basic lipids composing microcellular membranes. ³² Oxidation of PUFA can yield an array of bioactive oxygenated lipid mediators such as octadecanoids, eicosanoids, docosanoids, and other lipid metabolites. ³³ For example, oxidation of linoleic acid (LA) *via* the 15-lipoxygenase (15-LOX) or non-enzymatic pathway can produce two main classes of octadecanoids, hydroxy-octadecadienoic acid (HODE) and oxo-octadecadienoic acid (KODE). ^{33, 34} Our group has previously demonstrated that the defect-induced PL in SWCNTs can be achieved through photo-oxidation by lipid hydroperoxides. ⁷ We hypothesized that lipid hydroperoxides can photochemically oxidize SWCNTs resulting in the formation of ether functional groups on the SWCNT sidewalls. ⁷

In this work, we investigated the interaction between SWCNTs and linoleic-acidoxidative products, especially KODE and HODE. Compared to the previously reported linoleic acid hydroperoxides,⁷ these compounds are not strong oxidants, thus rendering them unlikely to generate similar oxygen-defects on the sidewalls of nanotubes. We found that these compounds can also photochemically react with SWCNTs through a $[2\pi + 2\pi]$ cycloaddition. The photochemical reaction results in a gradual increase of the red-shifted defect-induced PL (E_{11}^{-}) accompanied by the decrease of E_{11} under illumination. To further confirm the feasibility of proposed $[2\pi + 2\pi]$ cycloaddition doping in SWCNTs, we performed the reaction with shorter-chain commercially available organic compounds containing a carbonyl functional group with or without a conjugated carbon-carbon double bond. Our results indicate that 3decen-2-one, a class of α,β -unsaturated carbonyl compounds (enones), can effectively functionalize SWCNTs through $[2\pi + 2\pi]$ photocycloaddition. Density functional theory (DFT) calculations were performed to investigate the relative thermodynamic stability of a number of possible cycloadducts, including $[2\pi + 2\pi]$ and $[4\pi + 2\pi]$ products involving different C-C bonds on the chiral nanotube and products with different stereoselectivity. A detailed analysis on the steric repulsions and London dispersion interactions between the enone substrate and the SWCNT surface was performed to reveal factors that stabilize the $[2\pi + 2\pi]$ cycloadducts. While 1,3-dipolar and Diels-Alder cycloaddition reactions with carbon nanotubes and other carbon nanosurfaces have been studied extensively using computation to understand the origin of reactivity as well as regioselectivity of these transformations, $^{35-38}$ [$2\pi + 2\pi$] cycloadditions with SWCNTs are less explored computationally, 39,40 because they are usually kinetically less accessible. Additionally, most of the computational efforts have involved smaller organic substrates, without alkyl chain substituents, and in turn, the substituent effect on the chemoand regioselectivity has been overlooked. This photo-activated reaction enables creation of fluorescent quantum defects in SWCNTs through a controllable, facile, and inexpensive synthetic route.

Results and Discussion

The photo-activated reaction between SWCNTs and 9-KODE was conducted by irradiating the reaction mixture under 566 nm light. This wavelength corresponds to E₂₂ electronic transition in (6,5)-SWCNTs.¹ The selected wavelength is exclusive to SWCNTs, because 9-KODE does not absorb light at 566 nm, as shown by the absorption spectrum in Figure S1.

Figure 1a shows the excitation-emission (EE) maps of SWCNTs before and after reaction with 9-KODE for 1 h under illumination at 566 nm. Before the reaction (6,5)-SWCNTs displayed a characteristic bandgap E₁₁ emission at ~990 nm with 566 nm E₂₂ excitation, consistent with the previously reported fluorescence of (6,5)-SWCNTs.¹ The emission shoulders could be attributed to the photon sideband peak⁴¹⁻⁴³ and the remaining impurity of other SWCNT chiralities.⁴⁴ After 1 h illumination by resonant light at nanotube E₂₂ transition (566 nm), E₁₁ peak faded away and a red shifted E₁₁⁻ peak, centered at ~1114 nm, appeared accompanied by weak tail PL at longer wavelengths. It should also be noted that an even brighter PL peak centered at ~1114 nm emerged corresponding to the excitation by NIR light at E₁₁ transition of SWCNTs (Figure 1a, right panel). The PL intensity excited at E₁₁ is significantly higher compared to that excited at E₂₂ is the result of higher E₁₁ absorption intensity of SWCNTs. However, this feature is less obvious in pristine nanotube due to the overlap with Rayleigh scattering (Figure 1a, left panel). The Rayleigh scattering (diagonal

stripes on the upper-left corner of both EE maps in Figure 1a) is a result of the inherent optical filter configuration of the spectrofluorometer, the ineffectiveness of the equipped 830 nm long-pass filter to reject the scattered excitation light longer than 830 nm. Similar scattering effect has also been shown in the work using a 1150 nm long-pass filter. Figure 1b shows the spectra changes over 1 h photoreaction under 566 nm illumination, revealing the disappearance in the original E_{11} emission and gradual increase of two defect-induced PL peaks E_{11}^- and E_{11}^+ , centered at ~1114 nm and ~1255 nm, respectively. The existance of the isoemissive point at ~1050 nm is indicative of the direct conversion of the E_{11} emissive species to defect-induced emissive species, without the formation of an intermediate in the transition between them. $^{45-47}$

Figure 1c compares the UV-vis-NIR absorption spectra of reaction mixture at different time points under 566 nm irradiation. 9-KODE gives a characteristic absorption centered at 285 nm corresponding to the π to π^* transition of $\alpha,\beta-\gamma,\delta$ -diene ketone structure based on Woodward-Fieser rules. This peak decreased with the progress of the reaction and finally disappeared after 6 h irradiation; simultaneously a peak has appeared at ~230 nm with extended 6 h illumination. The ~55 nm blue-shift of the absorption indicates the complete consumption of 9-KODE with the destruction of the acyclic dienone structure and the formation of cyclobutane and/or oxetane ring. $^{51-54}$

The expanded inset in Figure 1c, showing vis-NIR absorbance of SWCNTs on a magnified scale, reveals E_{11} and E_{22} peaks drop by 21.1% and 3.7%, respectively, after treatment. The spectra change is analogous to those observed during oxygen⁸ and alkyl⁴ functionalization, which could be attributed to perturbations in the π -electron system from covalent doping. Besides, there is an obvious ~5 nm blue-shift at E_{11} transition after 6-h illumination. This observation can be correlated to the decreased length of the pristine, nonfunctionalized regions of SWCNTs as the reaction proceeds. When the defect-defect distance (Figure S2) shortens to sub-10 nm scale, this could cause increased quantum confinement effect along the SWCNTs.^{4,55,56} Figure 1d shows the changes of emission intensity of E_{11} , E_{11}^- , and E_{11}^+ peaks over 6-h 566 nm irradiation. The E_{11} emission decreased

monotonically within \sim 1 h of the reaction and then plateaued, while E_{11}^- intensity increased to a maximum after ~ 1 h and then subsequently decreased. The decline in E_{11}^- was caused by excessive functionalization after achieving optimal defect density on SWCNTs. The same observations were reported by Piao et al5 with diazonium functionalization. Notably, the intensity of the second red-shifted emission band, E₁₁*, concurrently changed at a rate slower than E_{11}^- . In contrast to the sharp drops of E_{11}^- by 63%, another defect-induce peak, E_{11}^* , only decreased by 23% after reaching its maximum. Here, similarly to previously reported dual redshifted emissions with alkyl¹³ and aryl²⁰ group functionalization, we observed the finite initial slopes of the time-dependent kinetic curves for E₁₁ and E₁₁ and significant slower decay rate of E_{11}^* compared to E_{11}^- . The above kinetic features of E_{11}^- and E_{11}^* more closely related to that of the parallel reactions than to the consecutive reactions.⁵⁷ Specifically, if E_{11}^- is an intermediate species and E₁₁* is the final product, the kinetic curve of E₁₁* would continue to increase after E₁₁⁻ species reaches its maximum at around 60 min. It could be thus inferred that E_{11} * emissive species, with a binding energy as high as ~260 meV, were formed in parallel processes to E_{11}^- emissive species rather than through sequential conversion of E_{11}^- sites into E₁₁* emitters.²⁰

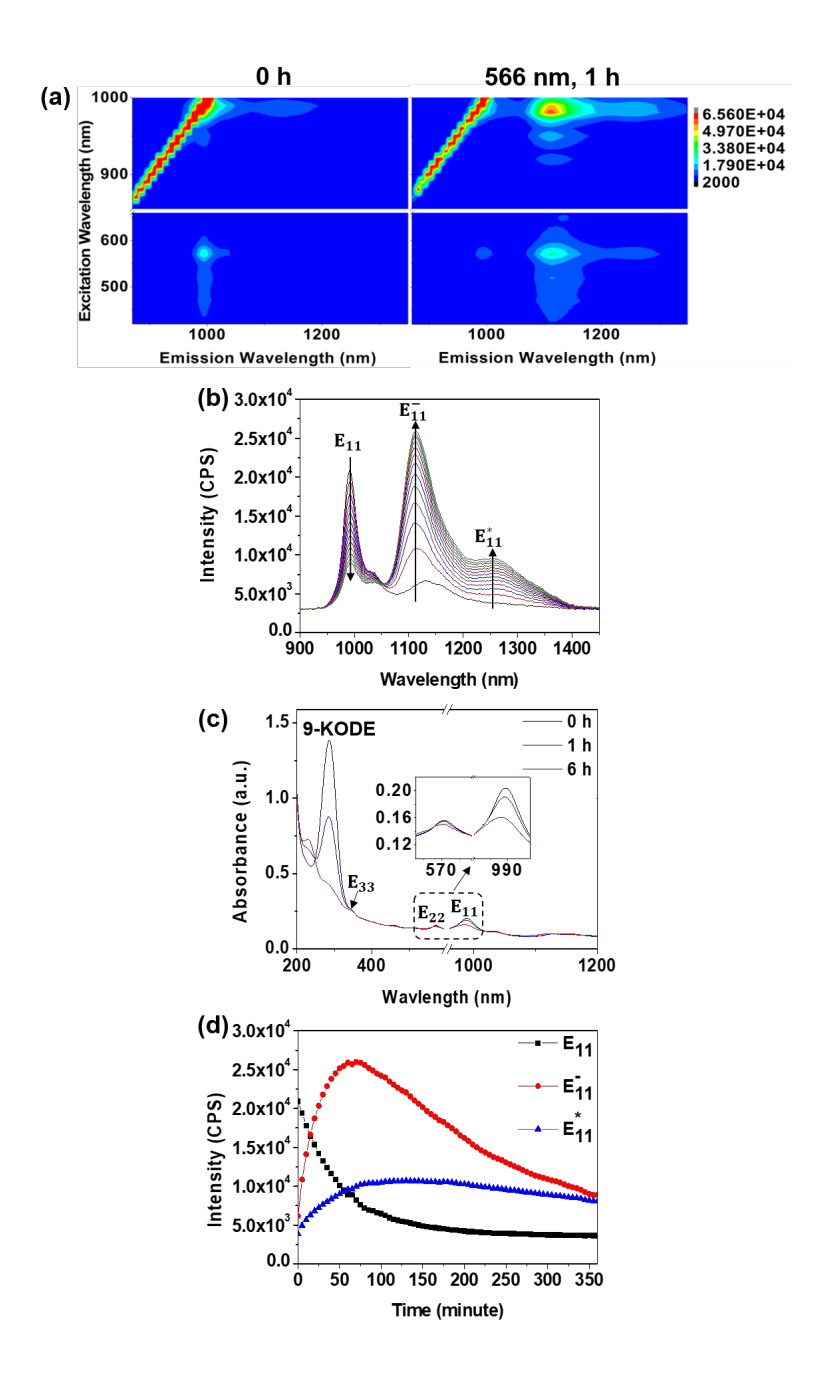


Figure 1. EE maps of SWCNTs (a) before and after 1 h reaction with 9-KODE under 566 nm illumination. (b) Fluorescent emission spectra change over 1 h (spectra taken every 5 min with 566 nm excitation). (c) UV-vis-NIR absorption spectra of the reaction mixture at different time points; expanded insets show E_{11} and E_{22} absorption peaks. (d) Emission intensities of E_{11} , E_{11}^- , and E_{11}^* of SWCNTs (with 566 nm excitation) reacted with 9-KODE over 6 h.

To ensure the observed effects were caused by the reaction between SWCNTs and 9-KODE, one control experiment was conducted without the addition of 9-KODE. As shown in Figure S3, after 1 h 566 nm irradiation, neither obvious E₁₁ decline nor evolution of both defect

peaks (E₁₁⁻ and E₁₁*) was observed. To confirm the doping was achieved through radical reactions, another control experiment was performed with radical scavengers, morin or ascorbic acid. When the reaction mixture was pretreated with radical scavenger to terminate any radical reactions, no enhancement of E₁₁⁻ and E₁₁* emission was observed (Figure S4). Moreover, saturated steric acid (18:0) without dienone functional group did not produce any spectra changes as well.7 Thus, it could be concluded that the produced red-shifted PL peaks were induced by photoinitiated radical reaction between SWCNTs and dienone structure in 9-KODE. Similar radical reaction mechanism has been proposed for other photochemical reactions aimed to generate the defects in SWCNTs.7, 15, 19, 20 In addition to 566 nm light activation, we also conducted the reaction under 285 nm illumination, resonant light to π to π^* transition in 9-KODE (Figure S1). In this reaction, the photoexcited species are 9-KODE instead of SWCNTs. 285 nm is beyond the E_{44} transition (~ 300 nm) of (6,5)-SWCNTs,⁴¹ at which the molar extinction coefficient of SWCNTs is order of magnitude lower than that of 9-KODE. 58-60 Similar approaches have been reported using UV light to excite only the dopants not the SWCNTs. 8, 20 Interestingly, we observed the emergence of the same defect-induced PL under 1h 285 nm illumination (Figure S5). The generated defect peaks, together with the corresponding energy shift, well matched those created under 1 h 566 nm illumination treatment (Table 1).

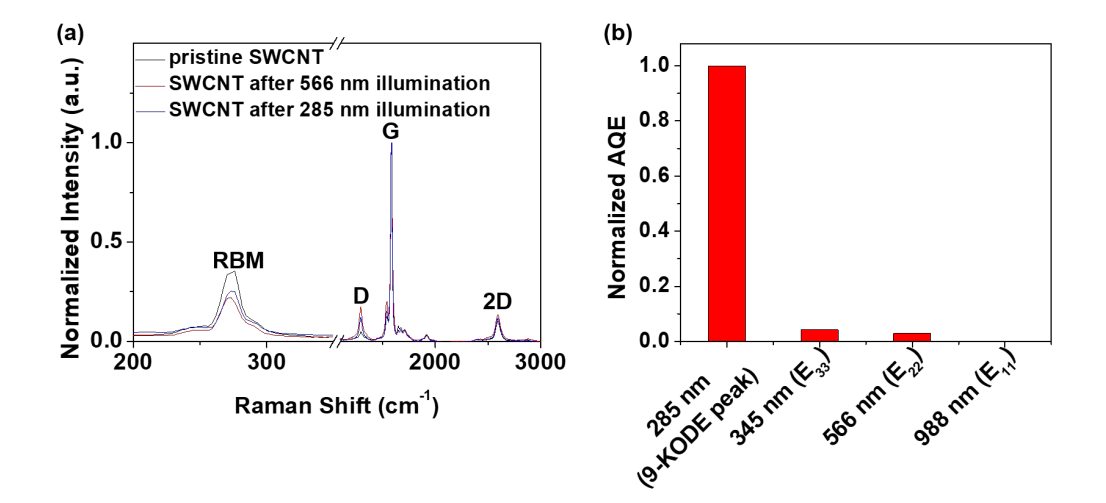


Figure 2. (a) Raman spectra of SWCNTs before and after reaction with 9-KODE under 6-h 566 nm and 285 nm illumination, respectively. (b) Normalized apparent quantum efficiency (AQE) of the reaction illuminated at different wavelengths (285, 345, 566, and 988 nm) for 1h. The emission spectra were recorded under 566 nm excitation before and after illumination.

The successful defect formation under both 566 nm and 285 nm illumination was further confirmed by Raman spectroscopy. Figure 2a shows the Raman spectra of SWCNTs with an increase of D/G ratio from 0.05 to 0.17 and 0.12 after 6-h reaction under 566 nm and 285 nm illumination, respectively. The rise in D/G ratio indicates the increased defect density of SWCNTs after reactions. The comparatively higher defect density after 566 nm irradiation, compared to 285 nm irradiation, is consistent with both PL emission and UV-vis-NIR absorption spectra (Figure 1 and Figure S5) due to more doping under 566 nm irradiation. The aforementioned results suggest that the mechanism of the reaction involves the excited state of either SWCNTs or 9-KODE as demonstrated by the effective E₁₁ formation at 566 nm and 285 nm excitation, respectively. Prior reports of light-assisted creation of fluorescent defects in SWCNTs involved the excitation of either nanotubes^{3,7,10,15,19} or dopants.^{6,8,20} Our light-driven functionalization of SWCNTs can be triggered *via* dual pathways under resonant excitation of both dopants and SWCNTs.

To further investigate the photochemical nature of the reaction between SWCNTs and 9-KODE, the reaction mixture was stored in dark for 1h. As shown in Figure S7, without irradiation, no evolvement of any defect PL peaks was observed. Besides, the action spectrum (Figure 2b) displaying the reaction efficiency at various illumination wavelength (285, 345, 566, and 988 nm) was also provided. Interestingly, we observed the highest reaction efficiency under 285 nm irradiation, the wavelength which matches the absorption band of 9-KODE (Figure S1), followed by the 345 nm illumination. This result further indicates that the doping reaction can be induced by direct excitation of either SWCNTs (E₂₂ and E₃₃ transitions) or 9-

KODE. The mechanism of the reaction involves the excited states of both SWCNTs and 9-KODE. Notably, under excitation energy corresponding to E₁₁ transition (988 nm) of (6,5)-SWCNTs, almost no defect PL evolved. The molar extinction coefficient of (6,5)-SWCNTs is the highest at 988 nm compared to 345 nm and 566 nm. The photon flux at 988 nm illumination is of the same order of magnitude as that at 566 nm illumination, and even orders of magnitude higher than that at 345 nm and 285 nm illumination (Table S2). However, the calculated apparent quantum efficiency (AQE) under 988 illumination is still three orders of magnitude lower compared to the highest AQE at 285 nm illumination (Table S2), which leads us to conclude that the photochemical reaction scarcely occurred at 988 illumination. The lack of functionalization under 988 nm was assumed to be a result of insufficient photon energy to overcome the reaction barrier.¹⁹

Here, in order to further explore the mechanism of observed photochemical reaction, we also performed similar photo-reaction under 1 h 566 nm illumination between SWCNTs and other 14 commercially available octadecanoids (Table S1). The ratio of the intensity of the defect-induced E_{11}^- peak (I_{11}^-) with respect to E_{11} peak (I_{11}), together with the energy shifts (ΔE) are shown in Table 1. 9-oxoODA and 13-KODE, similar to 9-KODE, have a diene structure conjugated to a carbonyl functional group. Thus, similar doping chemistry with ~135 meV energy shift was observed. The relative lower reaction efficiency of 9-oxoODA with respect to 9-KODE could be a result of the E-Z isomerization of diene functional group.⁶¹

The second group of compounds, HODE, compared with KODE group displayed a significant 10 meV higher energy shift with 145 meV, the defect PL further shifted to ~1120 nm. Besides, we also investigated the role of chirality on the reaction efficiency by testing both R- and S-HODE compounds (Table S1, data not shown). Our results indicated that the chirality of hydroxyl functional group did not affect the cycloaddition reaction with SWCNTs in terms of similar defect PL energy shifts and reaction efficiency.

The third group compounds, 10E,12Z-CLA and 9Z,11E-CLA, though remained the dienes functional group as those with HODE, missing the conjugated hydroxyl group.

Compared with HODE, similar energy shift at ~145 meV was observed, indicative of same type of cyclobutene ring formation with respect to HODE. However, the reaction between CLA and SWCNTs proceed at a much slower rate as shown by the low intensity ratio of 0.6 (Table 1). The less effective functionalization can be further confirmed by compared the intensity ratio with that before the reaction, namely for pristine SWCNTs, which is ~0.3. A similar effect has also been reported by Kwon *et al.*, who observed the dependence of E_{11}^- emission wavelengths and I_{11}^-/I_{11} ratios on different substituted (fluoro)alkyl/aryl sp³-defects. Linoleic acid oxidative products containing only one carbonyl group (3-oxo-stearic acid), or conjugated triene or tetraene groups (Table S1, No. 11-15) were also tested for reaction with SWCNTs under 1 h 566 illumination. As shown in Figure S8, no defect PL was observed.

Table 1. Comparison between different compounds after 1 h reaction with SWCNTs under 566 nm illumination.

Compound name	Skeletal structure	E ₁₁ (nm)	E ₁₁ ⁻ (nm)	ΔE (meV)	I ₁₁ -/I ₁₁
9-KODE		993	1114	135	3.2
9-KODE (285 nm illumination for 1 h)	О НО 12/2)	993	1112	134	0.9
9-oxoODA	O O (E)	991	1109	133	1.5
13-KODE	O HO 9(Z) (E) 13	993	1114	135	2.5
9R-HODE	O OH HO (E) (R) (E) 12(Z)	991	1121	145	1.0
13R-HODE	HO 9(Z) (E) (R) (3) OH	990	1120	145	1.4
10E,12Z-CLA	HO (E) (12(2)	991	1120	143	0.6
9Z,11E-CLA	O 9(Z) (E)	991	1121	145	0.6

Furthermore, we tested this reaction with other commercial enone compounds. Compared with PUFA compounds, these commercial enones are less expensive thus enabling potentially to scale up the synthesis of SWCNTs with quantum defects. Figure 3a shows the EE maps of SWCNTs before and after 1 h photoreaction with 3-decen-2-one under 566 nm illumination. A bright red-shifted PL peak centered at ~1126 nm with as high as 151 meV energy shift (Table 2) was appeared. Figure 3b showed the progressive spectra within 1 h reaction, which further confirmed the gradual increase of two defect-induced PL accompanied

by the decrease of original E_{11} peak. Figure 3c displayed the change of the UV-vis-NIR spectra over 6 h reaction. Consistent with previous results (Figure 1c), SWCNTs absorption peaks, especially at E_{11} transition, decreased progressively, demonstrating the successful functionalization of the SWCNTs. Besides, the shrinkage of the absorption peak at 300 nm due to n to π^* transition of enone functional group of 3-decen-2-one were indicative of the consumption of 3-decen-2one in the process. Kinetics curve (Figure 3d) showed the change of PL emission peak intensity over 6 h reaction. With the continuous decrease of the original E_{11} peak, two defect-induced PL peaks (E_{11}^- and E_{11}^*) gradually increased and then plateaued. Furthermore, reaction under illumination with 300 nm light, resonant with n to π^* transition of 3-decen-2-one absorption instead of SWCNTs, was performed. As shown in Figure S9 and Table 2, same defect-induced E_{11}^- peak centered at ~1127 nm with 154 meV energy shift appeared.

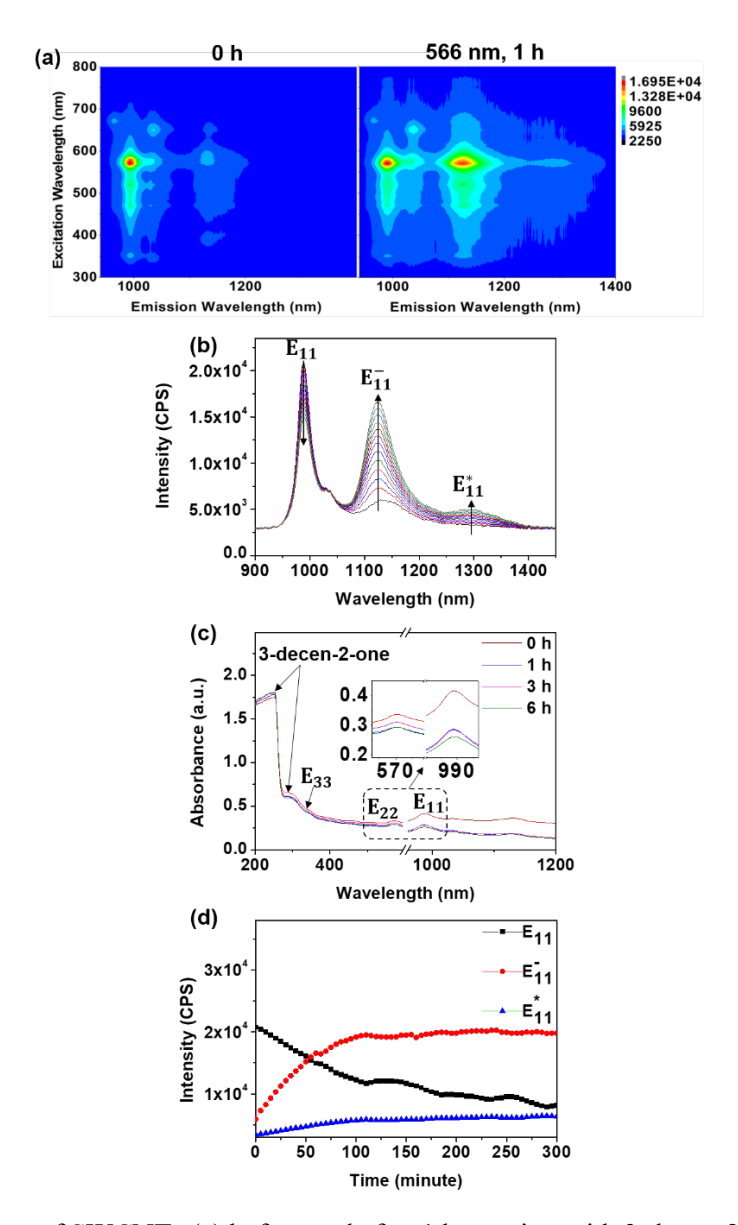


Figure 3. EE maps of SWCNTs (a) before and after 1 h reaction with 3-decen-2-one under 566 nm illumination. (b) Fluorescent emission spectra change over 1 h (spectra taken every 5 min with 566 nm excitation). (c) UV-vis-NIR absorption spectra of the reaction mixture at different time points; expanded insets show E_{11} and E_{22} absorption features. (d) Emission intensities of E_{11} , E_{11}^- , and E_{11}^+ of SWCNTs (with 566 nm excitation) reacted with 3-decen-2-one over 6 h.

We also compared 3-decen-2-one with other similar structure compounds (Table S1, No. 17-20) by their photo-induced reactivity with SWCNTs. As shown in Table 2, across all the tested compounds, 3-decen-2-one was the best in the emergence of the defect-induced PL as indicated by the highest I_{11}^-/I_{11} ratio of 1.1.

The reaction between SWCNTs and 3-octen-2-one, an organic molecule containing same enone functional group as 3-decen-2-one though with shorter 8-carbon chain length, proceeded at a very low efficiency. The intensity ratio I_{11} – I_{11} was only 0.39, barely increased compared with 0.3 for pristine SWCNTs. Furthermore, the reaction with another even shorter molecule 3-hepten-2-one under 1 h 566 nm irradiation did not induce any defect PL (Figure S10). Here, we believe the length of carbon chain played a determining role on the reaction efficiency with SWCNTs. Longer chain organic molecules have more favorable interactions with the hydrophobic surface of the nanotubes. Besides, when the reaction was initiated with the light that is resonant with the n to π^* of corresponding organic molecules, a radical of the organic molecules is formed. As the lifetime of radials is usually very short, longer chain molecules are more likely to react with the surfactant-wrapped SWCNTs more quickly before the radicals are quenched.

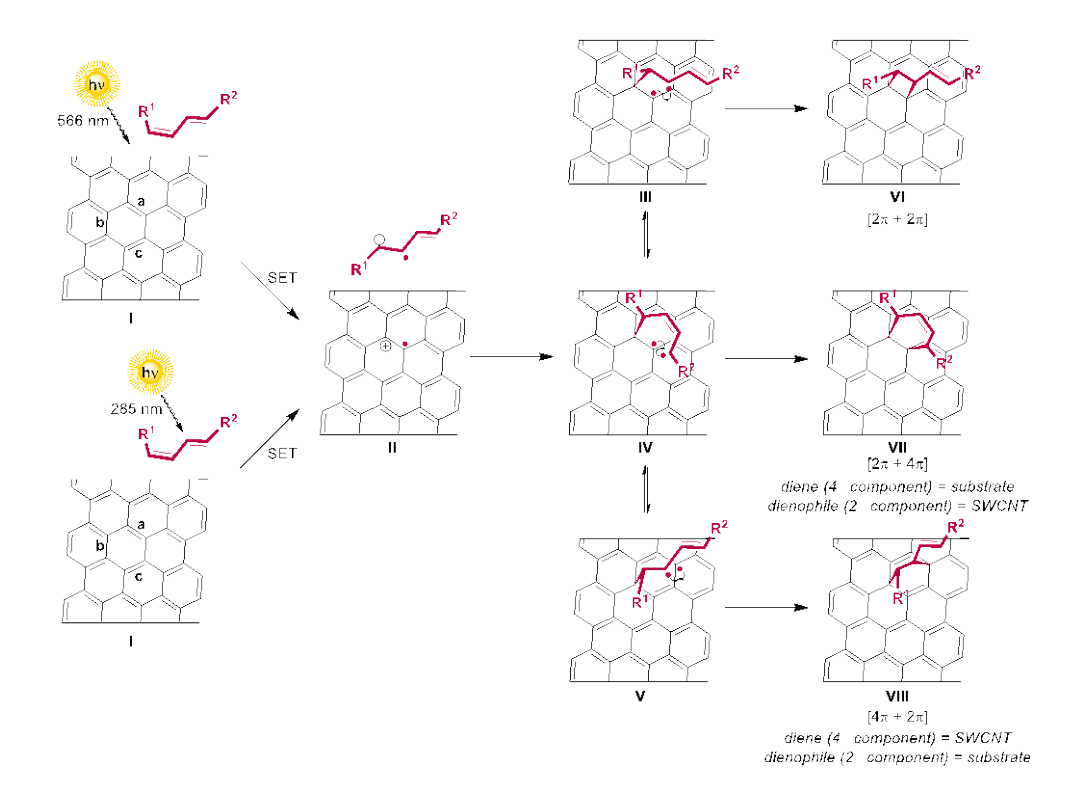
Two more compounds containing only keto functional groups, 2-decanone and 2-octanone, have been tested as well. As shown in Table 2, the reaction between SWCNTs and both molecules were slow under 566 nm illumination with intensity ratio of 0.49 and 0.46, respectively. This indicates that carbon-carbon double bonds can form four-membered ring structure with double bonds of SWCNTs more effectively than carbonyl groups through $[2\pi + 2\pi]$ photocycloaddition.

Table 2. Comparison between different compounds after 1 h reaction with SWCNTs.

Compound name	Skeletal structure	# of	Illumination	E_{11}	E_{11}^{-}	ΔΕ	I_{11}^-/I_{11}
		carbon	wavelength	(nm)	(nm)	(meV)	
3-decen-2-one	O (E)	10	566	990	1126	151	1.1
			300	988	1127	154	0.82
3-octen-2-one	0:	8	566	988	1130	157	0.39
	(E)		296	988	1130	157	0.39
2-decanone		10	566	988	1120	147	0.49
2-octanone	0	8	566	987	1121	150	0.46

Based on the experimental findings where the reaction was not observed under thermal conditions, as well as past studies on photo-functionalization of SWCNTs, 10, 19 we propose a reaction mechanism (Scheme 1) that involves initial single electron transfer (SET) from the photo-excited SWCNT to the enone substrate, or, alternatively, SET from SWCNT to the photo-excited enone, to generate a radical anion (II). The radical anion is rapidly trapped onto the SWCNT surface to form a C-C bond in a diradical intermediate (III, IV, or V). The subsequent C-C bond formation from the diradical intermediate may lead to several possible cycloaddition products, including the four-membered ring product (VI) via $[2\pi + 2\pi]$ cycloaddition and six-membered ring products (VII and VIII) via Diels-Alder ($[2\pi + 4\pi]$ or $[4\pi + 2\pi]$) cycloadditions where the substrate serves as the diene and the dienophile component, respectively. These stepwise cycloadditions are not expected to be stereospecific. Thus, either cis or trans stereoisomer may be formed in each pathway. Because different cycloaddition products (VI, VII, and VIII) are all formed via diradical intermediates (III, IV, and V) that are under rapid equilibrium, we expect that the product ratio is thermodynamically controlled and the relative energies of the cycloaddition products can be used to predict the major defect formed on the SWCNT surface.

Scheme 1. Proposed reaction mechanisms for generating different cycloaddition defects on (6,5) SWCNT.



We performed density functional theory (DFT) calculations to investigate the Gibbs free energies (ΔG) of the $[2\pi + 2\pi]$, $[2\pi + 4\pi]$ (substrate as diene), and $[4\pi + 2\pi]$ (substrate as dienophile) photocycloaddition products in the reaction between (6,5) SWCNT and (3E,5Z)-undecadiene-2-one (Table 3). Because there are three distinct types of C–C bonds on the SWCNT (bonds a-c, Scheme 1), cycloaddition products involving each of the three types of C–C bonds were calculated. Here, we define bond (a) and (c) as the C–C bonds relatively parallel to the axis of the nanotube and bond (b) as the C–C bonds nearly perpendicular to the axis. Furthermore, both cis and trans stereoisomers of the cycloaddition products and the diastereomers formed *via* addition of either of the prochiral faces of the alkene substrate were also considered (Table S3-S5). Our DFT calculations indicate that the $[2\pi + 2\pi]$ cycloaddition products are thermodynamically much more stable than the Diels-Alder products. The two most favorable products (1 and 3, Table 3) are formed *via* $[2\pi + 2\pi]$ cycloaddition with bonds (a) and (c) on the SWCNT, which are relatively parallel to the axis of the nanotube.

Table 3. Gibbs free energies (Δ G) of different cycloaddition products between photoexcited (6,5) SWCNT (with 566 nm light) and different substrates.^a

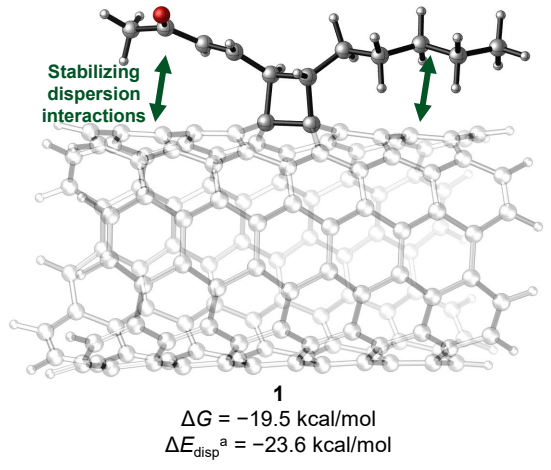
Substrate name	Substrate skeletal structure	Cycloaddition product ^b	ΔG (kcal/mol)
(3E,5Z)-undecadiene- 2-one		$[2\pi(a) + 2\pi(d)]$ (1)	-19.5
		$[2\pi(b) + 2\pi(d)]$ (2)	-16.0
	O d	$[2\pi(c) + 2\pi(d)]$ (3)	-18.4
		$[2\pi(a) + 4\pi(de)]$ (4)	-9.6
		$[2\pi(b) + 4\pi(de)]$ (5)	-11.3
		$[2\pi(c) + 4\pi(de)]$ (6)	-7.8
		$[4\pi(ab) + 2\pi(d)]$ (7)	-9.6
		$[4\pi(ac) + 2\pi(d)]$ (8)	50.2
		$[4\pi(bc) + 2\pi(d)]$ (9)	-2.3
ethylene	<u>d</u>	$[2\pi(a) + 2\pi(d)]$ (10)	-25.6
	<u></u>	$[2\pi(b) + 2\pi(d)]$ (11)	-25.8
1,3-butadiene	\\d e//	$[2\pi(a) + 4\pi(de)]$ (12)	-27.5
		$[2\pi(b) + 4\pi(de)]$ (13)	-25.7

^a See Tables S3-S5 for energies of the less stable stereoisomers in each reaction pathway. ^b See Scheme 1 for the three different types of C-C bonds (a-c) on the SWCNT surfaces involved in the cycloadditions.

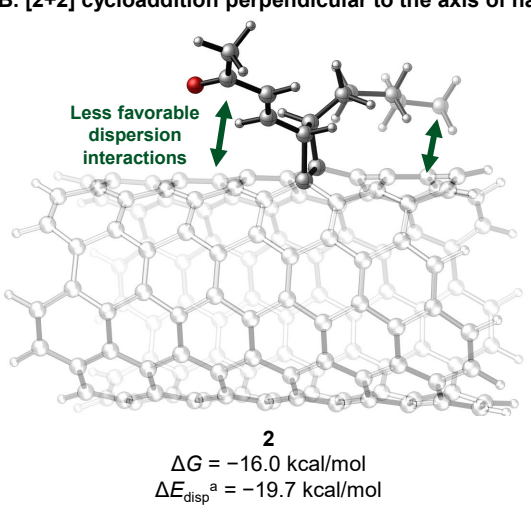
Analysis of the steric repulsion and attractive London-dispersion interactions between the substrate and the nanotube surface revealed multiple factors that affect the stability of the $[2\pi + 2\pi]$ and Diels-Alder products. In the most stable $[2\pi + 2\pi]$ cycloaddition products (1 and 3, Table 3) the alkenyl and alkyl substituents on the four-membered ring can align along with

the axis of the nanotube and are stabilized by London-dispersion interactions (Figure 4A). The addition to the perpendicular bond on SWCNT (*i.e.* product **2**, Figure 4B) places the alkenyl and alkyl substituents are further away from the SWCNT surface due to the perpendicular alignment, leading to decrease in the favorable dispersion interactions between the nanotube and the substrate. Furthermore, all Diels-Alder adducts are sterically more demanding, due to the formation of a six-membered ring, as opposed to a smaller four-membered ring. The Diels-Alder adducts are destabilized due to steric repulsions between the alkenyl and acyl substituents and the SWCNT surface.

A. [2+2] cycloaddition parallel to the axis of nanotube



B. [2+2] cycloaddition perpendicular to the axis of nanotube



C. Most favorable Diels-Alder cycloaddition product

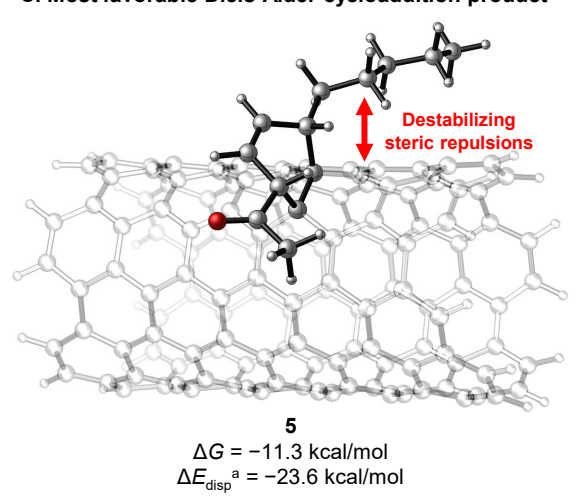


Figure 4. Structures and energies of representative $[2\pi + 2\pi]$ cycloaddition and Diels-Alder products. ^a Dispersion energies (ΔE_{disp}) between SWCNT and the substituents on the cycloadduct were calculated using Grimme's DFT-D3 method from the dispersion-free HF functional.62

The analysis above suggests that the $[2\pi + 2\pi]$ cycloadducts 1 and 3 are stabilized due to attractive dispersion interactions with the substituents on the four-membered ring, while the Diels-Alder adducts are destabilized by steric repulsions with the substituents. To further test this hypothesis and elucidate substituent effects on product stability, we compared the reaction energies of model $[2\pi + 2\pi]$ cycloadditions with an unsubstituted ethylene and Diels-Alder reactions with 1,3-butadiene (Table 3). Our results indicate that the two $[2\pi + 2\pi]$ cycloadducts with ethylene added to either bond (a) (10, Table 3) or bond (b) (11, Table 3) on SWCNT have similar energies ($\Delta G = -25.6$ and -25.8 kcal/mol, respectively). These results highlight the significance of the substituents on the olefin to stabilize regioisomers 1 and 3 as compared to 2 (Table 3). To further understand the origin of this difference, we computed the attractive dispersion interaction energies between the alkyl and alkenyl substituents on the cyclobutane and the nanotube. Adduct 1 has substantially larger dispersion interactions between the nanotube and the substituents than adduct 2 ($\Delta\Delta E_{\rm disp} = -3.9$ kcal/mol) (Figure 4). This difference is consistent with the relative stabilities between these two product isomers ($\Delta\Delta G =$ -3.5 kcal/mol, Table 3). The Diels-Alder cycloaddition of unsubstituted butadiene and SWCNT is slightly more exergonic than the $[2\pi + 2\pi]$ cycloaddition with ethylene. These results suggest that the lower stability of Diels-Alder adducts 4-6 as compared to $[2\pi + 2\pi]$ adducts (1 and 3) are due to substituent effects that lead to greater steric repulsions with the SWCNT and the loss of enone conjugation in the Diels-Alder adducts 4-6.

Table 4. Reaction energies to form different cycloaddition products and reduction potential of substrates.

	Substrate skeletal structure	ΔG (kc	Substrate	
Substrate name		Most favorable $[2\pi + 2\pi]$ product	Diradical intermediate	reduction potential ^a (V vs SCE)
(3E,5Z)- undecadiene-2-one	O (E) (Z)	-19.5^{b}	-10.9	-1.58
2-hydroxy-(3E,5Z)- undecadiene	OH (E) (Z)	-23.1 ^b	-9.8	-2.68
(3E,5Z)- undecadiene	(E) (Z)	-22.1^{b}	-10.4	-2.92
2-undecanone		-1.6 ^c	6.1	-2.85

^a See SI for computational details of the reduction potential calculations. Single point energy calculations for reduction potentials were performed at the PBE-D3-6-311++G(d,p)/SMD(water) level of theory. ^b Cycloaddition between Z alkene and bond **a** on SWCNT. ^c Cycloaddition between carbonyl and bond **c** on SWCNT.

With the understanding of the $[2\pi + 2\pi]$ cycloadducts as the major product of the photocycloaddition, we investigated factors that may contribute to the observed reactivity trend of different substrates. Based on the experimental intensity ratios (I_{11} – I_{11} , Table 1), it was apparent that dienone (KODEs) was more reactive than α -hydroxy-diene (HODEs), which was more reactive than unsubstituted diene (CLAs). To investigate the origin of the reactivity, we calculated the energies of $[2\pi + 2\pi]$ cycloadducts and diradical intermediates in reactions with substrates (3E,5Z)-undecadiene-2-one, 2-hydroxy-(3E,5Z)-undecadiene, (3E,5Z)-undecadiene, and 2-undecanone (Table 4). (Because the geometries of open-shell singlet diradicals cannot be successfully located in our geometry optimizations after multiple attempts, h., geometry optimizations of the diradical intermediates were performed at triplet state. Single point energies were then computed as an open shell singlet). In reactions with

(3E,5Z)-undecadiene-2-one, 2-hydroxy-(3E,5Z)-undecadiene, and (3E,5Z)-undecadiene, formation of both the cycloadduct and the diradical intermediate are highly exergonic, and experimental reactivity trends do not correlate with the exergonicity. On the other hand, the computed reduction potentials of these substrates have good correlation with the observed reactivity trend. The reduction of dienone, (3E,5Z)-undecadiene-2-one, was significantly more favorable than the reduction of α-hydroxy-diene, 2-hydroxy-(3E,5Z)-undecadiene. The reduction of unsubstituted diene, (3E,5Z)-undecadiene, is the least favorable. The difference in reduction potential can be attributed to the relative stability of the radical anion, where the anion in dienone is better stabilized by resonance resulting in a large difference in reduction potential and reactivity. On the other hand, the difference between diene and α -hydroxy-diene is less significant, and the difference can be attributed to the stabilization of the negative charge by an inductive effect with and electron withdrawing hydroxy group on the α carbon. These results suggest that the rates of these reactions are affected by the initial single electron transfer to the substrate. Finally, we investigated the addition of 2-undecanone to SWCNT. This reaction is much less exergonic and involves a less stable diradical intermediate than the reactions with dienone, (3E,5Z)-undecadiene-2-one (Table 4). Therefore, the low reactivity of 2-decanone and 2-octanone (Table 2) can be attributed to the thermodynamically disfavored formation of the oxetane product.

Conclusions

We demonstrated that oxidative products of linoleic acid, particularly KODE and HODE, can efficiently functionalization the sp² carbon lattice of SWCNTs at ambient conditions through $[2\pi + 2\pi]$ photocycloaddition. The reaction occurs in aqueous solution at room temperature upon mixing the compounds with nanotubes in the presence of light. Notably, the sidewall cycloaddition can occur through two-sided photo excitation, with resonant excitation of either the nanotubes with visible light or the compounds with UV light. The aqueous medium also allows for *in situ* probing the evolution of the sidewall cycloaddition and provides a molecular level control. The observed chemistry of molecular engineering the

surface of SWCNTs provides understanding of the reaction between SWCNTs and lipids, and can be potentially applied to *in vivo* lipid detection.

More importantly, this exciton-tailoring chemistry is not limited to 18-carbon fatty acid but also applicable to shorter enone-containing organic molecules with only 10-carbon length. The reaction efficiency largely depends on the chain length, while remains low with molecules containing only keto functional group. These findings provide a more economical and potentially scalable way to synthesis SWCNTs as being single-photon emitters.

Our computational results further supported the above proposed $[2\pi + 2\pi]$ photocycloaddition mechanism by comparing the stability of the products with those through $[2\pi + 4\pi]$ photocycloaddition. Additionally, dispersion interactions and steric effects were found to play key role in determining chemo- and regionselectivity of the reaction with SWCNTs. Products involved C=C pointing along the axis of SWCNTs are more favorable compared with those pointing perpendicular to the axis.

Materials and Methods

Cobalt-molybdenum-catalyzed (CoMoCAT) single-walled (6,5) carbon nanotubes were purchased from Sigma-Aldrich (SG65, 0.7-0.9 nm diameter) and used without further purification. Morin hydrate and ascorbic acid were also purchased from Sigma-Aldrich.

SWCNT suspensions were prepared at 0.5 mg/mL with 0.5 wt % sodium cholate (SC, Sigma-Aldrich) as a surfactant in nanopure water. The suspensions were sonicated for 1 h and centrifuged at 7000 rpm for 30 min (Centrifuge 5804, Eppendorf) to remove large SWCNT bundles. The top 90% of the supernatant was transferred to a separate container and used as stock.

The prepared surfactant-coated SWCNT stock solution was diluted 25 times, and mixed with either 170 μ M of a series of 18-carbon fatty acids (Table S1, No. 1–15) or 20 mM of each No. 16–20 compounds (Table S1). Samples were illuminated with 566 nm light at a power density of 6.13 mW/cm² for 60 min unless stated otherwise.

NIR photoluminescence measurements were performed on a Nanolog spectrofluorometer (HORIBA Jobin Yvon) equipped with a xenon lamp (400 W) light source, double excitation monochromators, and Symphony II InGaAs array (NIR) detector. Spectra were obtained using 566 nm excitation wavelength, which is in resonance with the first absorption band of the (6,5) SWCNTs. Slit widths were set at 10 nm for both excitation and emission. All measurements were obtained with an 830 nm long-pass filter at ambient temperature. Power density was measured independently with an optical power meter (Thorlabs PM200) and detector (Thorlabs S120VC). Power densities at different illumination wavelengths for the reactions are available in Table S2.

UV-vis-NIR absorption spectra were obtained using PerkinElmer Lambda 900 spectrophotometer over the wavelength range of 200–1200 nm.

Raman spectra were acquired on XploRA plus confocal Raman microscope (Horiba) with 638 nm laser (24 mW) operating at 10% power.

All the DFT calculations were carried out by using the GAUSSIAN 16 program.⁶³ Full geometry optimizations were performed with the PBE⁶⁴ functional with Grimme's D3 dispersion correction⁶⁵ and the split-valence 3-21G basis set. Single-point energy calculations on the PBE-D3-optimized geometries were performed in water using the SMD solvation model⁶⁶ at the PBE-D3/6-31G(d) level of theory, with thermal corrections to Gibbs free energies calculated by harmonic vibration frequency analysis at the PBE-D3/3-21G level of theory. A 15 angstrom nanotube was generated using Avogadro,^{67,68} and terminal carbons were capped using hydrogens. To ensure 15 angstrom model was sufficient for this study, electronic energies of key structures were also calculated using longer (50 Å) nanotube model (Table S7). Single point energy calculations for reduction potentials were performed at the PBE-D3/6-311++G(d,p) level of theory in water using the SMD solvation model.

ASSOCIATED CONTENT

Supporting Information

The Supporting Information is available free of charge at

Full list of compounds tested; UV-vis-NIR absorption and photoluminescence data of

SWCNTs and/or different compounds under various conditions; kinetics of the

photochemical reaction; details of the wavelength-dependence experiments; three

dimensional structures and computed reaction energies of different diastereomers;

comparison of Gibbs free energies and electronic energies of key cycloadducts (PDF)

Calculated coordinates (XYZ)

AUTHOR INFORMATION

Corresponding Author

Alexander Star

Email: astar@pitt.edu

Acknowledgements

This material is based upon work supported by the National Science Foundation under

Grant No. 2003302 and the National Institutes of Health under Grant No. R35GM128779. I.K.

thanks Pittsburgh Quantum Institute for graduate fellowship. DFT calculations were conducted

at the Center for Research Computing at the University of Pittsburgh, the Extreme Science and

Engineering Discovery Environment (XSEDE), and the TACC Frontera Supercomputer.

References

1. Bachilo, S. M.; Strano, M. S.; Kittrell, C.; Hauge, R. H.; Smalley, R. E.; Weisman, R. B.

Structure-Assigned Optical Spectra of Single-Walled Carbon Nanotubes. Science 2002, 298,

2361-2366.

2. O'Connell, M. J.; Bachilo, S. M.; Huffman, C. B.; Moore, V. C.; Strano, M. S.; Haroz, E.

H.; Rialon, K. L.; Boul, P. J.; Noon, W. H.; Kittrell, C.; Ma, J.; Hauge, R. H.; Weisman, R.

B.; Smalley, R. E. Band Gap Fluorescence from Individual Single-Walled Carbon Nanotubes.

Science 2002, 297, 593-596.

25

- 3. Ghosh, S.; Bachilo, S. M.; Simonette, R. A.; Beckingham, K. M.; Weisman, R. B. Oxygen Doping Modifies Near-Infrared Band Gaps in Fluorescent Single-Walled Carbon Nanotubes. *Science* **2010**, *330*, 1656-1659.
- 4. Zhang, Y.; Valley, N.; Brozena, A. H.; Piao, Y. M.; Song, X. P.; Schatz, G. C.; Wang, Y.
 H. Propagative Sidewall Alkylcarboxylation that Induces Red-Shifted Near-IR
 Photoluminescence in Single-Walled Carbon Nanotubes. J. Phys. Chem. Lett. 2013, 4, 826-830.
- 5. Piao, Y. M.; Meany, B.; Powell, L. R.; Valley, N.; Kwon, H.; Schatz, G. C.; Wang, Y. H. Brightening of Carbon Nanotube Photoluminescence through the Incorporation of sp³ Defects. *Nat. Chem.* **2013**, *5*, 840-845.
- 6. Iizumi, Y.; Yudasaka, M.; Kim, J.; Sakakita, H.; Takeuchi, T.; Okazaki, T. Oxygen-Doped Carbon Nanotubes for Near-Infrared Fluorescent Labels and Imaging Probes. *Sci. Rep.* **2018**, *8*, 6272.
- 7. Chiu, C. F.; Saidi, W. A.; Kagan, V. E.; Star, A. Defect-Induced Near-Infrared Photoluminescence of Single-Walled Carbon Nanotubes Treated with Polyunsaturated Fatty Acids. *J. Am. Chem. Soc.* **2017**, *139*, 4859-4865.
- 8. Lin, C. W.; Bachilo, S. M.; Zheng, Y.; Tsedev, U.; Huang, S. N.; Weisman, R. B.; Belcher, A. M. Creating Fluorescent Quantum Defects in Carbon Nanotubes using Hypochlorite and Light. *Nat. Commun.* **2019**, *10*, *2874*.
- Deng, S.; Zhang, Y.; Brozena, A. H.; Mayes, M. L.; Banerjee, P.; Chiou, W.-A.; Rubloff,
 W.; Schatz, G. C.; Wang, Y. Confined Propagation of Covalent Chemical Reactions on
 Single-Walled Carbon Nanotubes. *Nat. Commun.* 2011, 2, 382.
- 10. Kwon, H.; Furmanchuk, M.; Kim, M.; Meany, B.; Guo, Y.; Schatz, G. C.; Wang, Y. H., Molecularly Tunable Fluorescent Quantum Defects. *J. Am. Chem. Soc.* **2016**, *138*, 6878-6885.

- 11. Maeda, Y.; Takehana, Y.; Yamada, M.; Suzuki, M.; Murakami, T. Control of the Photoluminescence Properties of Single-Walled Carbon Nanotubes by Alkylation and Subsequent Thermal Treatment. *Chem. Commun.* **2015**, *51*, 13462-5.
- 12. Maeda, Y.; Kuroda, K.; Tambo, H.; Murakoshi, H.; Konno, Y.; Yamada, M.; Zhao, P.; Zhao, X.; Nagase, S.; Ehara, M. Influence of Local Strain Caused by Cycloaddition on the Band Gap Control of Functionalized Single-Walled Carbon Nanotubes. *RSC Adv.* **2019**, *9*, 13998-14003.
- 13. Brozena, A. H.; Leeds, J. D.; Zhang, Y.; Fourkas, J. T.; Wang, Y. Controlled Defects in Semiconducting Carbon Nanotubes Promote Efficient Generation and Luminescence of Trions. *ACS Nano* **2014**, *8*, 4239-4247.
- 14. Kwon, H.; Kim, M.; Nutz, M.; Hartmann, N. F.; Perrin, V.; Meany, B.; Hofmann, M. S.; Clark, C. W.; Htoon, H.; Doorn, S. K.; Hoegele, A.; Wang, Y. H. Probing Trions at Chemically Tailored Trapping Defects. *ACS Cent. Sci.* **2019**, *5*, 1786-1794.
- 15. Powell, L. R.; Piao, Y.; Wang, Y. Optical Excitation of Carbon Nanotubes Drives Localized Diazonium Reactions. *J. Phys. Chem. Lett.* **2016**, *7*, 3690-3694.
- 16. Shiraki, T.; Shiraishi, T.; Juhasz, G.; Nakashima, N. Emergence of New Red-Shifted Carbon Nanotube Photoluminescence Based on Proximal Doped-Site Design. *Sci. Rep.* **2016**, *6*, 28393.
- 17. Zheng, Y.; Bachilo, S. M.; Weisman, R. B. Controlled Patterning of Carbon Nanotube Energy Levels by Covalent DNA Functionalization. *ACS Nano* **2019**, *13*, 8222-8228.
- 18. Powell, L. R.; Kim, M.; Wang, Y. Chirality-Selective Functionalization of Semiconducting Carbon Nanotubes with a Reactivity-Switchable Molecule. *J. Am. Chem. Soc.* **2017**, *139*, 12533-12540.

- 19. Wu, X. J.; Kim, M.; Kwon, H.; Wang, Y. H. Photochemical Creation of Fluorescent Quantum Defects in Semiconducting Carbon Nanotube Hosts. *Angew. Chem. Int. Ed.* **2018**, *57*, 648-653.
- 20. Zheng, Y.; Bachilo, S. M.; Weisman, R. B. Photoexcited Aromatic Reactants Give Multicolor Carbon Nanotube Fluorescence from Quantum Defects. *ACS Nano* **2020**, *14*, 715-723.
- 21. Luo, H. B.; Wang, P.; Wu, X.; Qu, H.; Ren, X.; Wang, Y. One-Pot, Large-Scale Synthesis of Organic Color Center-Tailored Semiconducting Carbon Nanotubes. *ACS Nano* **2019**, *13*, 8417-8424.
- 22. Brozena, A. H.; Kim, M.; Powell, L. R.; Wang, Y., Controlling the Optical Properties of Carbon Nanotubes with Organic Colour-Centre Quantum Defects. *Nat. Rev. Chem.* **2019**, *3*, 375-392.
- 23. Shiraki, T.; Miyauchi, Y.; Matsuda, K.; Nakashima, N. Carbon Nanotube Photoluminescence Modulation by Local Chemical and Supramolecular Chemical Functionalization. *Acc. Chem. Res.* **2020**, *53*, 1846-1859.
- 24. He, X. W.; Hartmann, N. F.; Ma, X. D.; Kim, Y.; Ihly, R.; Blackburn, J. L.; Gao, W. L.; Kono, J.; Yomogida, Y.; Hirano, A.; Tanaka, T.; Kataura, H.; Htoon, H.; Doorn, S. K. Tunable Room-Temperature Single-Photon Emission at Telecom Wavelengths from sp(3) Defects in Carbon Nanotubes. *Nat. Photonics* **2017**, *11*, 577-582.
- 25. Akizuki, N.; Aota, S.; Mouri, S.; Matsuda, K.; Miyauchi, Y. Efficient Near-Infrared Up-Conversion Photoluminescence in Carbon Nanotubes. *Nat. Commun.* **2015**, *6*, 8920.
- 26. Miyauchi, Y.; Iwamura, M.; Mouri, S.; Kawazoe, T.; Ohtsu, M.; Matsuda, K. Brightening of Excitons in Carbon Nanotubes on Dimensionality Modification. *Nat. Photonics* **2013**, *7*, 715-719.

- 27. Ma, X. D.; Hartmann, N. F.; Baldwin, J. K. S.; Doorn, S. K.; Htoon, H. Room-Temperature Single-Photon Generation from Solitary Dopants of Carbon Nanotubes. *Nat. Nanotechnol.* **2015**, *10*, 671-675.
- 28. He, X.; Htoon, H.; Doorn, S. K.; Pernice, W. H. P.; Pyatkov, F.; Krupke, R.; Jeantet, A.; Chassagneux, Y.; Voisin, C. Carbon Nanotubes as Emerging Quantum-Light Sources. *Nat. Mater.* **2018**, *17*, 663-670.
- 29. Kwon, H.; Kim, M.; Meany, B.; Piao, Y.; Powell, L. R.; Wang, Y. Optical Probing of Local pH and Temperature in Complex Fluids with Covalently Functionalized, Semiconducting Carbon Nanotubes. *J. Phys. Chem. C* **2015**, *119*, 3733-3739.
- 30. Hartmann, N. F.; Velizhanin, K. A.; Haroz, E. H.; Kim, M.; Ma, X. D.; Wang, Y. H.; Htoon, H.; Doorn, S. K. Photoluminescence Dynamics of Aryl sp³ Defect States in Single-Walled Carbon Nanotubes. *ACS Nano* **2016**, *10*, 8355-8365.
- 31. Sykes, M. E.; Kim, M.; Wu, X.; Wiederrecht, G. P.; Peng, L.; Wang, Y.; Gosztola, D. J.; Ma, X. Ultrafast Exciton Trapping at sp³ Quantum Defects in Carbon Nanotubes. *ACS Nano* **2019**, *13*, 13264-13270.
- 32. Shaikh, S. R.; Edidin, M. Polyunsaturated Fatty Acids and Membrane Organization: Elucidating Mechanisms to Balance Immunotherapy and Susceptibility to Infection. *Chem. Phys. Lipids* **2008**, *153*, 24-33.
- 33. Astarita, G.; Kendall, A. C.; Dennis, E. A.; Nicolaou, A. Targeted Lipidomic Strategies for Oxygenated Metabolites of Polyunsaturated Fatty Acids. *Biochim. Biophys. Acta* **2015**, *1851*, 456-68.
- 34. Raftery, D. Mass Spectrometry in Metabolomics: Methods and Protocols; Springer: New York, 2014.

- 35. Li, Y.; Osuna, S.; Garcia-Borràs, M.; Qi, X.; Liu, S.; Houk, K. N.; Lan, Y., Reactivity of Single-Walled Carbon Nanotubes in the Diels-Alder Cycloaddition Reaction: Distortion-Interaction Analysis along the Reaction Pathway. *Chem. Eur. J.* **2016**, *22*, 12819-12824.
- 36. Mercuri, F.; Sgamellotti, A. First-Principles Investigations on the Functionalization of Chiral and Non-Chiral Carbon Nanotubes by Diels-Alder Cycloaddition Reactions. *Phys. Chem. Chem. Phys.* **2009**, *11*, 563-567.
- 37. Osuna, S. L.; Houk, K. N. Cycloaddition Reactions of Butadiene and 1,3-Dipoles to Curved Arenes, Fullerenes, and Nanotubes: Theoretical Evaluation of the Role of Distortion Energies on Activation Barriers. *Chem. Eur. J.* **2009**, *15*, 13219-13231.
- 38. Lu, X.; Tian, F.; Wang, N.; Zhang, Q. Organic Functionalization of the Sidewalls of Carbon Nanotubes by Diels-Alder Reactions: A Theoretical Prediction. *Org. Lett.* **2002**, *4*, 4313-4315.
- 39. Cao, Y.; Osuna, S.; Liang, Y.; Haddon, R. C.; Houk, K. N. Diels-Alder Reactions of Graphene: Computational Predictions of Products and Sites of Reaction. *J. Am. Chem. Soc.* **2013**, *135*, 17643-17649.
- 40. Martínez, J. P.; Langa, F.; Bickelhaupt, F. M.; Osuna, S.; Solà, M. (4 + 2) and (2 + 2) Cycloadditions of Benzyne to C₆₀ and Zig-Zag Single-Walled Carbon Nanotubes: The Effect of the Curvature. *J.Phys. Chem. C* **2016**, *120*, 1716-1726.
- 41. Wei, X.; Tanaka, T.; Yomogida, Y.; Sato, N.; Saito, R.; Kataura, H. Experimental Determination of Excitonic Band Structures of Single-Walled Carbon Nanotubes Using Circular Dichroism Spectra. *Nat. Commun.* **2016**, *7*, 12899.
- 42. Torrens, O. N.; Zheng, M.; Kikkawa, J. M. Energy of K-Momentum Dark Excitons in Carbon Nanotubes by Optical Spectroscopy. *Phys. Rev. Lett.* **2008**, *101*, 157401.

- 43. Blackburn, J. L.; Holt, J. M.; Irurzun, V. M.; Resasco, D. E.; Rumbles, G. Confirmation of K-Momentum Dark Exciton Vibronic Sidebands Using ¹³C-labeled, Highly Enriched (6,5) Single-walled Carbon Nanotubes. *Nano Letters* **2012**, *12* (3), 1398-1403.
- 44. Weisman, R. B.; Bachilo, S. M. Dependence of Optical Transition Energies on Structure for Single-Walled Carbon Nanotubes in Aqueous Suspension: An Empirical Kataura Plot. *Nano Letters* **2003**, *3*, 1235-1238.
- 45. Koti, A. S. R.; Krishna, M. M. G.; Periasamy, N. Time-Resolved Area-Normalized Emission Spectroscopy (TRANES): A Novel Method for Confirming Emission from Two Excited States. *J. Phys. Chem. A* **2001**, *105*, 1767-1771.
- 46. Fujimoto, K.; Shimizu, H.; Inouye, M. Unambiguous Detection of Target DNAs by Excimer–Monomer Switching Molecular Beacons. *J. Org. Chem.* **2004**, *69*, 3271-3275.
- 47. Iwamura, M.; Takeuchi, S.; Tahara, T. Real-Time Observation of the Photoinduced Structural Change of Bis(2,9-dimethyl-1,10-phenanthroline)copper(I) by Femtosecond Fluorescence Spectroscopy: A Realistic Potential Curve of the Jahn–Teller Distortion. *J. Am. Chem. Soc.* **2007**, *129* (16), 5248-5256.
- 48. Woodward, R. B. Structure and the Absorption Spectra of α,β-Unsaturated Ketones. *J. Am. Chem. Soc.* **1941**, *63* (4), 1123-1126.
- 49. Fieser, L. F.; Fieser, M.; Rajagopalan, S. Absorption Spectroscopy and the Structure of the Diosterols. *J. Org. Chem.* **1948**, *13*, 800-806.
- 50. Woodward, R. B. Structure and Absorption Spectra. III. Normal Conjugated Dienes. *J. Am. Chem. Soc.* **1942**, *64*, 72-75.
- 51. Medishetty, R.; Tandiana, R.; Koh, L. L.; Vittal, J. J. Assembly of 3D Coordination Polymers from 2D Sheets by [2+2] Cycloaddition Reaction. *Chem. –Eur. J.* **2014**, *20*, 1231-1236.

- 52. Kancheva, P. B.; Delchev, V. B. Investigation of the Mechanisms of Photo-Induced Formation of Cyclobutane Dimers of Cytosine and 2,4-Diaminopyrimidine. *J. Mol. Model.* **2016,** *22*, 230.
- 53. Sonoda, Y. Solid-State [2+2] Photodimerization and Photopolymerization of α, ω -Diarylpolyene Monomers: Effective Utilization of Noncovalent Intermolecular Interactions in Crystals. *Molecules* **2010**, *16*, 119-148.
- 54. Fedorova, O. A.; Saifutiarova, A. E.; Gulakova, E. N.; Guskova, E. O.; Aliyeu, T. M.; Shepel, N. E.; Fedorov, Y. V. The Regioselective [2 + 2] Photocycloaddition Reaction of 2-(3,4-Dimethoxystyryl)quinoxaline in Solution. *Photochem. Photobiol. Sci.* **2019**, *18*, 2208-2215.
- 55. Sun, X.; Zaric, S.; Daranciang, D.; Welsher, K.; Lu, Y.; Li, X.; Dai, H. Optical Properties of Ultrashort Semiconducting Single-Walled Carbon Nanotube Capsules Down to Sub-10 nm. *J. Am. Chem. Soc.* **2008**, *130*, 6551-6555.
- 56. He, X.; Gifford, B. J.; Hartmann, N. F.; Ihly, R.; Ma, X.; Kilina, S. V.; Luo, Y.; Shayan, K.; Strauf, S.; Blackburn, J. L.; Tretiak, S.; Doorn, S. K.; Htoon, H. Low-Temperature Single Carbon Nanotube Spectroscopy of sp³ Quantum Defects. *ACS Nano* **2017**, *11*, 10785-10796.
- 57. El Seoud, O. A.; Baader, W. J.; Bastos, E. L. Practical Chemical Kinetics in Solution. Encyclopedia of Physical Organic Chemistry 2016, 1-68.
- 58. Schöppler, F.; Mann, C.; Hain, T. C.; Neubauer, F. M.; Privitera, G.; Bonaccorso, F.; Chu, D.; Ferrari, A. C.; Hertel, T. Molar Extinction Coefficient of Single-Wall Carbon Nanotubes. *J. Phys. Chem. C* 2011, *115*, 14682-14686.
- 59. Sanchez, S. R.; Bachilo, S. M.; Kadria-Vili, Y.; Lin, C.-W.; Weisman, R. B. (n,m)-Specific Absorption Cross Sections of Single-Walled Carbon Nanotubes Measured by Variance Spectroscopy. *Nano Letters* **2016**, *16*, 6903-6909.

- 60. Kühn, H.; Wiesner, R.; Rathmann, J.; Schewe, T. Formation of Ketodienoic Fatty Acids by the Pure Pea Lipoxygenase-1. *Eicosanoids* **1991,** *4*, 9-14.
- 61. Cai, W.; Fan, H.; Ding, D.; Zhang, Y.; Wang, W. Synthesis of Z-alkenes *via* Visible Light Promoted Photocatalytic E → Z Isomerization under Metal-Free Conditions. *Chem. Commun.* **2017,** *53*, 12918-12921.
- 62. Roothaan, C. C. J. New Developments in Molecular Orbital Theory. *Revi.Mod. Phys.* **1951**, 23, 69-89.
- 63. Frisch, M. J.; Trucks, G. W.; Schlegel, H. B.; Scuseria, G. E.; Robb, M. A.; Cheeseman, J. R.; Scalmani, G.; Barone, V.; Petersson, G. A.; Nakatsuji, H.; Li, X.; Caricato, M.; Marenich, A. V.; Bloino, J.; Janesko, B. G.; Gomperts, R.; Mennucci, B.; Hratchian, H. P.; Ortiz, J. V.; Izmaylov, A. F.; *et al.* Gaussian 16 Rev. C.01, Wallingford, CT, 2016.
- 64. Perdew, J. P.; Burke, K.; Ernzerhof, M. Generalized Gradient Approximation Made Simple. *Phys. Rev. Lett.* **1996,** *77*, 3865-3868.
- 65. Grimme, S.; Antony, J.; Ehrlich, S.; Krieg, H. A Consistent and Accurate *ab Initio* Parametrization of Density Functional Dispersion Correction (DFT-D) for the 94 Elements H-Pu. *J. Chem. Phys.* **2010**, *132*, 154104.
- 66. Marenich, A. V.; Cramer, C. J.; Truhlar, D. G. Universal Solvation Model Based on Solute Electron Density and on a Continuum Model of the Solvent Defined by the Bulk Dielectric Constant and Atomic Surface Tensions. *J. Phys. Chem. B* **2009**, *113*, 6378-6396.
- 67. Hanwell, M. D.; Curtis, D. E.; Lonie, D. C.; Vandermeersch, T.; Zurek, E.; Hutchison, G. R. Avogadro: An Advanced Semantic Chemical Editor, Visualization, and Analysis Platform. *J. Cheminf.* **2012**, *4*, 17.
- 68. Avogadro: An Open-Source Molecular Builder and Visualization Tool. Version 1.2.0 http://avogadro.cc/. (accessed January 05, 2021)

TOC

